

The Merger Rates and Mass Assembly Histories of Dark Matter Haloes in the Two Millennium Simulations

Onsi Fakhouri^{1*}, Chung-Pei Ma¹, and Michael Boylan-Kolchin²

¹*Department of Astronomy, 601 Campbell Hall, University of California, Berkeley, CA 94720*

²*Max-Planck-Institut für Astrophysik, Karl-Schwarzschild-Str. 1, 85748 Garching, Germany*

23 October 2018

ABSTRACT

We construct merger trees of dark matter haloes and quantify their merger rates and mass growth rates using the joint dataset from the Millennium and Millennium-II simulations. The finer resolution of the Millennium-II Simulation has allowed us to extend our earlier analysis of halo merger statistics to an unprecedentedly wide range of descendant halo mass ($10^{10} \lesssim M_0 \lesssim 10^{15} M_\odot$), progenitor mass ratio ($10^{-5} \lesssim \xi \lesssim 1$), and redshift ($0 \leq z \lesssim 15$). We update our earlier fitting form for the mean merger rate *per halo* as a function of M_0 , ξ , and z . The overall behavior of this quantity is unchanged: the rate per unit redshift is nearly independent of z out to $z \sim 15$; the dependence on halo mass is weak ($\propto M_0^{0.13}$); and it is nearly a power law in the progenitor mass ratio ($\propto \xi^{-2}$). We also present a simple and accurate fitting formula for the mean mass growth rate of haloes as a function of mass and redshift. This mean rate is $46 M_\odot \text{ yr}^{-1}$ for $10^{12} M_\odot$ haloes at $z = 0$, and it increases with mass as $\propto M^{1.1}$ and with redshift as $(1+z)^{2.5}$ (for $z \gtrsim 1$). When the fit for the mean mass growth rate is integrated over a halo’s history, we find excellent match to the mean mass assembly histories of the simulated haloes. By combining merger rates and mass assembly histories, we present results for the number of mergers over a halo’s history and the statistics of the redshift of the last major merger.

1 INTRODUCTION

Mergers of dark matter haloes are intimately connected to a wide array of phenomena in the now-standard Λ CDM cosmology. In addition to being the dominant channel for mass growth of haloes themselves, mergers are also responsible for the growth of stellar mass in galaxies, both directly via galaxy-galaxy mergers, and indirectly via the accretion of potentially star-forming gas. Furthermore, mergers help shape many important observational properties of galaxies, e.g., star formation rates, color and morphology transformations, dynamical states of stellar disks, and galaxy mass and luminosity functions. Mergers are also responsible for the existence of satellite galaxies such as dwarf spheroidals in the Milky Way and non-cD galaxies in galaxy clusters. Quantifying the rate of halo-halo mergers, and its possible dependence on factors such as halo mass, mass ratio, and time, is therefore of great interest for a theoretical understanding of galaxy formation and its connections to observations.

In a series of papers, we have examined various aspects of the growth of dark matter haloes. In Fakhouri & Ma (2008), we computed the merger rates of dark matter haloes from the Millennium Simulation (Springel et al. 2005) and presented a simple algebraic fitting form for our results. The resolution and size of this simulation allowed us to determine the merger rate over the parameter range of $10^{12} \lesssim M_0 \lesssim 10^{15} M_\odot$ for the mass of the descendant haloes, $10^{-3} \lesssim \xi \lesssim 1$ for the mass ratio of the progenitor haloes,

and $0 \leq z \lesssim 6$ for the redshift. The detailed environmental dependence of the merger rates and halo mass growths was analyzed in two subsequent papers (Fakhouri & Ma 2009, 2010). In McBride et al. (2009), we studied the statistics of the halo mass assembly histories and mass growth rates in the Millennium Simulation. Halo mergers have also been studied in a handful of papers by others (e.g., Governato et al. 1999; Gottlöber et al. 2001; Berrier et al. 2006; Maller et al. 2006; Guo & White 2008; Genel et al. 2009; Stewart et al. 2009). The pre-2008 studies were all limited to small simulations that mainly investigated major mergers in a narrow mass range at low redshift (typically $z \lesssim 1$). Some such studies have emphasized potential challenges for hierarchical structure formation; for instance, Stewart et al. (2008) have noted that the frequency of major mergers among Milky-Way sized haloes poses a problem for thin-disk survivability. Much work has also been done in quantifying halo mass accretion and assembly histories using N -body simulations that are smaller than the Millennium runs (e.g., Lacey & Cole 1994; Tormen et al. 1997; Tormen 1998; Wechsler et al. 2002; van den Bosch 2002; Li et al. 2007; Zhao et al. 2009, except Cole et al. 2008).

In this paper, we extend the results presented in Fakhouri & Ma (2008) and McBride et al. (2009) by incorporating the Millennium-II Simulation (Boylan-Kolchin et al. 2009). This simulation has the same number of particles as the Millennium Simulation but has 125 times better mass resolution. This new database provides 7.5×10^6

dark matter haloes (each containing more than 1000 simulation particles) between redshift 0 and 15 and their subhalo merger trees for our analysis. Adding to the 11.3×10^6 haloes (between $z = 0$ and 6) available from the Millennium Simulation, this combined dataset allows us to determine the dark matter halo merger rates and mass growth rates from $z = 0$ to up to $z = 15$, for over five orders of magnitude in the descendant halo mass ($10^{10} \lesssim M_0 \lesssim 10^{15} M_\odot$) and progenitor mass ratio ($10^{-5} \lesssim \xi \leq 1$).

This paper is organized as follows. Section 2 describes the dark matter haloes in the Millennium and Millennium-II simulations, and how we construct the merger trees and quantify the merger statistics and mass accretion histories of the haloes. In Section 3, we present results for three types of statistics: merger rates at $z = 0$ up to ~ 15 for halo mass $\sim 10^{10}$ to $10^{15} M_\odot$ (§ 3.1); the rate at which the haloes are accreting dark matter across the virial radii, and the mass growth history of haloes (§ 3.2); and the cumulative merger statistics over a halo’s past history, e.g., the mean cumulative number of mergers of a given mass ratio experienced as a function of z and halo mass, and the distribution of the redshift at which the last major merger occurred for haloes at various mass and redshift (§ 3.3). The Appendix contains a detailed comparison of the three types of algorithms that we have tested for handling the fragmentation events in a merger tree of FOF haloes (Fakhouri & Ma 2008, 2010). They are named “snip,” “stitch,” and “split,” depending on whether the fragmented subhalo was ignored, stitched back to the original FOF halo in subsequent outputs, or split off from the FOF at earlier times. A quantitative assessment of the systematic differences in the merger rates derived from each algorithm is provided in the Appendix.

The cosmology used throughout this paper is identical to that used in the the Millennium simulations: a Λ CDM model with $\Omega_m = 0.25$, $\Omega_b = 0.045$, $\Omega_\Lambda = 0.75$, $h = 0.73$, an initial power-law index $n = 1$, and $\sigma_8 = 0.9$. Masses and lengths are quoted in units of M_\odot and Mpc without the Hubble parameter h .

2 CONSTRUCTION OF HALO MERGER TREES

2.1 The Two Millennium Simulations

The Millennium and Millennium-II simulations are large N -body simulations of cosmological structure formation using the concordance Λ CDM cosmological parameters listed at the end of Section 1. The simulations are described in detail in Springel et al. (2005) (Millennium) and Boylan-Kolchin et al. (2009) (Millennium-II); here we summarize some basic features of the simulations and of the default post-processing procedures that result in subhalo merger trees.

Both simulations follow the evolution of $2160^3 \approx 10^{10}$ particles from redshift 127 to redshift 0 using versions of the GADGET tree-PM code (Springel et al. 2001; Springel 2005). The simulations differ in spatial scale and mass resolution: the Millennium Simulation uses a box size of $L = 685$ Mpc and a Plummer-equivalent force softening that is a factor of 10^5 smaller, $\epsilon = 6.85$ kpc, with a particle mass of $m_p = 1.18 \times 10^9 M_\odot$. The Millennium-II Simulation uses $L = 137$ Mpc and $\epsilon = 1.37$ kpc, both of which are a fac-

tor of 5 smaller than the values from the Millennium Simulation; the particle mass is therefore 125 times smaller, $m_p = 9.43 \times 10^6 M_\odot$. The two simulations have 60 outputs at identical redshifts between $z \approx 20$ and $z = 0$, spaced approximately equally in $\log z$, as well as additional snapshots (4 for the Millennium, 8 for the Millennium-II) at higher redshifts.

Subhalo merger trees are constructed in an identical fashion for the Millennium and Millennium-II simulations. Dark matter haloes are first identified at each snapshot using a Friends-of-Friends group-finder (FOF; Davis et al. 1985) with a linking length of 0.2 times the mean interparticle separation. All FOF groups with at least 20 particles are stored. The SUBFIND algorithm (Springel et al. 2001) is then applied to each FOF group to identify halo substructure. SUBFIND identifies local density maxima and performs an unbinding procedure to determine which particles in the FOF group are bound to each density peak. Substructures with at least 20 particles after unbinding are stored, resulting in a list of subhaloes (SHs) associated with each FOF group in the simulation. Note that some FOF groups do not contain 20 self-bound particles and therefore not every FOF group contains a subhalo, while some FOF groups can contain many self-bound density peaks and therefore have many subhaloes.

These subhaloes are then linked across simulation snapshots to produce subhalo merger trees. This linking is done by establishing a unique descendant for each subhalo in the following manner. First, all particles in the subhalo are rank-ordered by binding energy. A list of candidate descendants – all subhaloes at the subsequent snapshot containing at least one particle from the subhalo in question – is built and a figure of merit is computed for each descendant. The candidate descendant with the highest score is assigned as the actual descendant. The figure of merit for candidate descendants is simply a weighted sum of the rank-ordering of the subhalo’s particles; this procedure ensures that the tightly bound center of a subhalo is weighted more heavily than the less-bound outer regions even if the center is subdominant in terms of mass.

In addition to searching for a descendant at the subsequent output, a search is also performed two snapshots later. This additional step accounts for subhaloes that are temporarily unresolved when passing near the center of a more massive system but re-appear later. On occasion, no descendant can be identified at either of the two subsequent snapshots, in which case, the subhalo is not assigned a descendant at all but rather is considered destroyed. With subhaloes and their unique descendants identified, subhalo merger trees are built by linking subhaloes and their descendants: all subhaloes with a common descendant at $z = 0$ are linked to all subhaloes sharing these subhaloes as descendants, and so on. A given subhalo merger tree thus contains all subhaloes that can be linked via their descendants to one specific subhalo at $z = 0$. The trees link 760 million subhaloes for the Millennium Simulation and 590 million subhaloes for the Millennium-II Simulation. For the central subhalo of a $z = 0$ galaxy-mass halo ($M \approx 10^{12} M_\odot$), its subhalo merger tree typically consists of 90 subhaloes in the Millennium Simulation and 2800 subhaloes in the Millennium-II Simulation.

$z_p:z_d$	Sim	$10^{10}-10^{11}M_\odot$		$10^{11}-10^{12}M_\odot$		$10^{12}-10^{13}M_\odot$		$10^{13}-10^{14}M_\odot$		$>10^{14}M_\odot$		Total
		$N_p = 1$	$N_p \geq 2$	$N_p = 1$	$N_p \geq 2$	$N_p = 1$	$N_p \geq 2$	$N_p = 1$	$N_p \geq 2$	$N_p = 1$	$N_p \geq 2$	
0.12:0.06	M	0	0	0	0	321,489	90,922	14,504	45,281	3	4,817	477,016
	M-II	214,045	25,292	12,583	17,107	13	3,279	0	486	0	36	272,841
0.56:0.51	M	0	0	0	0	306,142	98,664	11,442	39,469	0	2,757	458,474
	M-II	224,865	29,170	12,422	18,405	7	3,199	0	421	0	20	288,509
1.17:1.08	M	0	0	0	0	236,280	137,729	4,197	32,349	0	976	411,531
	M-II	220,703	49,811	8,473	23,221	1	2,985	0	316	0	8	305,518
2.23:2.07	M	0	0	0	0	126,926	133,965	629	12,746	0	73	274,339
	M-II	202,572	80,435	4,772	24,874	2	2,128	0	121	0	0	314,904

Table 1. The number of merger events in the two Millennium simulations at four representative redshifts ($z \approx 0, 0.5, 1, \text{ and } 2$). At each z , we list the number of descendant FOF haloes that have a single progenitor halo ($N_p = 1$, i.e., no mergers) and multiple progenitors ($N_p \geq 2$), for five descendant mass bins (left to right). The descendant mass here refers to the halo mass at the redshift listed rather than at the present day. Only haloes containing more particles than our minimum cutoff (1000 for descendants; 40 for progenitors) are counted. The higher-resolution Millennium-II Simulation dominates the contribution to the merger statistics of $M_0 \lesssim 10^{12}M_\odot$ haloes, while the larger-volume Millennium Simulation dominates the contribution to cluster-mass haloes.

2.2 Halo Fragmentation

In this paper, as in our previous work (Fakhouri & Ma 2008; McBride et al. 2009), our focus is on the merger and assembly histories of FOF haloes. To do this we must first construct merger trees of the FOF haloes from the underlying subhalo trees described in Section 2.1. Such construction is nontrivial due to halo fragmentations: subhaloes of a progenitor FOF halo may have descendants that reside in more than one FOF halo. Sometimes this is due to a physical unbinding event in which a subhalo formerly bound to an FOF is ejected out of the FOF system. Sometimes the fragmentation is spurious – a subhalo may oscillate in and out of the FOF group before finally settling in. Sometimes the FOF algorithm incorrectly groups subhaloes that are unbound but only happen to pass by one another and should not be associated as a single FOF group.

We presented detailed comparisons in Fakhouri & Ma (2008, 2010) of three types of algorithms – snip, stitch, and split – for handling these fragmentation events. In the Appendix we summarize these algorithms and quantify the systematic differences in the merger rates derived from each algorithm.

For the main results presented in § 3 below, we use the split-3 algorithm, in which the subhalo fragments that pop out of an FOF halo are either snipped or split depending on a simple criterion. The fragmented subhalo is snipped if it is observed to remain in the FOF halo for all 3 snapshots immediately preceding the fragmentation event; in this case the ancestral link between fragment and FOF is severed. If the fragmented subhalo is not in the FOF halo for all 3 preceding snapshots, it is interpreted as distinct and is split off from the FOF. The split-3 algorithm generally gives very similar results to the stitch-3 algorithm used in Fakhouri & Ma (2008), e.g., the two methods produce merger rates that agree to within 10% for the redshifts and mass ranges that we have statistics for. The only exception is in the major merger regime for low-mass haloes at low redshift ($z \lesssim 1$), where split-3 is lower than stitch-3 by up to 30% (see Fig. 10 in Appendix). Overall, split-3 appears slightly more robust at handling spurious FOF linking events in this regime (also see Fakhouri & Ma 2010; Genel et al. 2009). As discussed in the Appendix, however, the exact definition of what consti-

tutes a merger may be situation-dependent, meaning that no single method is perfect in all cases.

2.3 Extracting Merger Rates and Mass Accretion Histories

From the merger trees of FOF haloes obtained by applying a given fragmentation algorithm, we extract a merger catalog. Each catalog provides us with a list of descendant FOF haloes at redshift $z_d \geq 0$ with mass M_0 , and for each descendant halo, its set of N_p FOF progenitors at $z_p = z_d + \Delta z$, where N_p can range from 1 (i.e. a single progenitor) to a large number, depending on the halo mass and the value of Δz . We label the rank-ordered progenitor mass with M_i , $i \in (1, 2, \dots, N_p)$, and $M_1 \geq M_2 \geq \dots M_{N_p}$. To ensure that only numerically resolved haloes are included in our study, we impose a minimum of 1000 particles for the descendant haloes and 40 particles for the progenitor haloes. For the Millennium Simulation, this criterion corresponds to a minimum halo mass of $1.2 \times 10^{12}M_\odot$ for the descendant and $4.7 \times 10^{10}M_\odot$ for the progenitor. For Millennium-II, the minimum masses are $9.4 \times 10^9M_\odot$ and $3.8 \times 10^8M_\odot$ for the descendant and progenitor haloes. We emphasize that the mass of a descendant halo refers to its mass at a given redshift z_d and not its ultimate mass at $z = 0$ (unless $z_d = 0$).

We compute the merger rates at redshift z as a function of descendant mass M_0 and progenitor mass ratio $\xi = M_i/M_1$ (for $i > 1$). We define $B(M_0, \xi, z)$ to be the number of mergers per Mpc^3 , dM_0 , $d\xi$, and Δz with mass $M_0 \pm dM_0/2$ and mass ratio $\xi \pm d\xi/2$. As discussed in Fakhouri & Ma (2008), we find the mean merger rate *per halo*, $B(M_0, \xi, z)/n(M_0, z) \equiv dN_m/d\xi/dz$, where $n(M_0, z)$ is the number density of haloes, to have a particularly simple dependence on the merger parameters. This rate, when expressed in per redshift units, is a dimensionless quantity that gives the mean number of mergers per halo per unit z per unit ξ . To avoid artificial boundary effects at $z = 0$, we use the two outputs at $z = 0.12$ and 0.06 to compute the $z \sim 0$ merger rate.

To compute the mass accretion histories and accretion rates of haloes, we start with a given descendant FOF halo at some redshift and identify the mass of its most massive

progenitor at an earlier snapshot. This process is iterated backwards in time to construct the main branch of the descendant's merger tree. The mass trajectory along the main branch of a descendant gives us its mass accretion history $M(z)$ (see. e.g., Lacey & Cole 1993), from which we can compute the mass accretion rate \dot{M} as a function of z . Note that the progenitor halo on the main branch of a descendant halo at a given snapshot need not be the most massive progenitor of that descendant at that snapshot.

2.4 Definitions of Halo Mass

In our prior analysis of the Millennium halo merger rate (Fakhouri & Ma 2008), we assigned the halo mass using the standard FOF mass M_{FOF} . This mass is simply proportional to the number of particles assigned to each FOF halo by the FOF group finder. An alternative definition that we will use throughout this paper is the sum of the masses of an FOF's subhaloes, M_{SH} . This definition has been shown recently by Genel et al. (2009) to be more robust than M_{FOF} since the SUBFIND algorithm assigns only gravitationally bound particles to each subhalo.

Overall, we find the halo mass functions computed using these two mass definitions to differ at the 5% level at all halo masses. This difference can be caused by a slight excess of mass in FOF haloes due to unbound or spuriously linked particles, as well as by a slight deficit in M_{SH} when SUBFIND does not account for all the mass physically associated with a subhalo. When restricted to the subset of haloes that are undergoing very minor mergers, however, Genel et al. (2009) noted that the FOF mass of the smaller progenitor increases as it approaches the more massive progenitor. For minor mergers involving mass ratios as low as $\xi \sim 0.001$, the ratio $M_{\text{FOF}}/M_{\text{SH}}$ for the *smaller* progenitor can rise from 1.03 to 1.5 prior to mergers. We will therefore use M_{SH} for halo masses in this study. We note that this discrepancy occurs only for the small subset of low-mass haloes that are in the process of merging onto a much larger halo; its effect on the total halo mass function is therefore limited to $\sim 5\%$.

3 RESULTS

To provide a sense for the halo statistics and merger events available from the two Millennium simulations, we list in Table 1 the number of descendant haloes (above 1000 particles) and their progenitors (above 40 particles) at four representative redshifts for five broad mass ranges from 10^{10} to $> 10^{14} M_{\odot}$. The results presented below are based on these events and those at other redshifts.

3.1 Merger Rates

3.1.1 Present-Day Merger Rates

The left panel of Fig. 1 presents $B(M_0, \xi, z = 0)$, the $z = 0$ mean number of mergers per unit volume, descendant mass M_0 , mass ratio ξ , and redshift as a function of progenitor mass ratio ξ from the two Millennium simulations (solid for Millennium II; dashed for Millennium). The colored curves correspond to different mass bins ranging from $10^{10} M_{\odot}$ (blue) to $10^{16} M_{\odot}$ (red). The rates are determined from the

$z = 0.06$ and 0.12 merger tree catalogue since, as described in Section 2.3, we would like to avoid the $z = 0.0$ snapshot due to the boundary effects that interfere with the post-processing algorithms used to handle the halo fragmentation events. The split-3 algorithm is used here; other algorithms yield qualitatively similar agreement between the two simulations (see Appendix for details).

The right panel of Fig. 1 shows the mean merger rate per halo, $B/n = dN_m/d\xi/dz$, where each of the curves in the left panel has been divided by the number density of haloes in that mass bin. The collapse of the curves to nearly a single curve shows that the per halo merger rate $dN_m/d\xi/dz$ is nearly independent of halo mass. This collapse is similar to that seen in Fig. 6 of Fakhouri & Ma (2008) for the Millennium Simulation. A comparison of the two figures helps illustrate the large dynamic range achieved when the two Millennium simulations are combined: the halo mass range has been increased by two orders of magnitude in Fig. 1, and for each mass bin, the progenitor mass ratio is extended downward by also a factor of ~ 100 , reaching $\xi \sim 10^{-6}$ for $M_0 = 10^{15} M_{\odot}$.

The overlap in the merger parameter space between the two simulations is seen to be fairly small in Fig. 1. The two simulations are therefore quite complementary: Millennium II allows us to probe descendant and progenitor masses that are a factor of 125 smaller than Millennium, whereas the larger box of the Millennium Simulation provides robust statistics for the rare events that are poorly sampled in Millennium II, e.g., major mergers of massive haloes (i.e. the lower right corner of left panel of Fig. 1). Over the small region of overlap, Fig. 1 shows good agreements between the merger rates determined from the two simulations: both the power-law dependence on ξ and the weak dependence on M_0 carry over from Millennium to Millennium II. Boylan-Kolchin et al. (2009) show that many other quantities, such as halo mass functions, formation times, and subhalo abundances, have a much wider range of overlap and that the two simulations are in excellent agreement for these quantities as well.

The weak dependence of the merger rate on M_0 is shown explicitly in Fig. 2. Each curve here shows the mean rate per halo, $dN_m/d\xi/dz$, integrated over different ranges of $\xi \geq \xi_{\text{min}}$, where $\xi_{\text{min}} = 0.3, 0.10, 0.01$, and 10^{-3} (from bottom up). Major mergers with mass ratio within 1:3 (bottom curve) are clearly much more rare than minor mergers (top curves), but all the curves have very similar power-law dependence on M_0 . Over about 4.5 orders of magnitude in M_0 , the rate increases by only a factor of ~ 3 , suggesting that the merger rate scales roughly as $\sim M_0^{0.1}$. A more accurate fit is provided in Sec 3.1.3 below.

3.1.2 $z > 0$ Merger Rates

The Millennium Simulation provided sufficient halo statistics for us to determine the halo merger rates up to $z \sim 6$ in our previous study. The higher mass resolution of the Millennium-II Simulation now allows us to probe redshifts up to ~ 15 . The combined results from the two simulations are shown in Fig. 3, which plots the mean merger rate per unit redshift (left panel), dN_m/dz , and per unit time (right panel), dN_m/dt , as a function of redshift. These merger rates have been integrated over different ranges of $\xi \geq \xi_{\text{min}}$, rang-

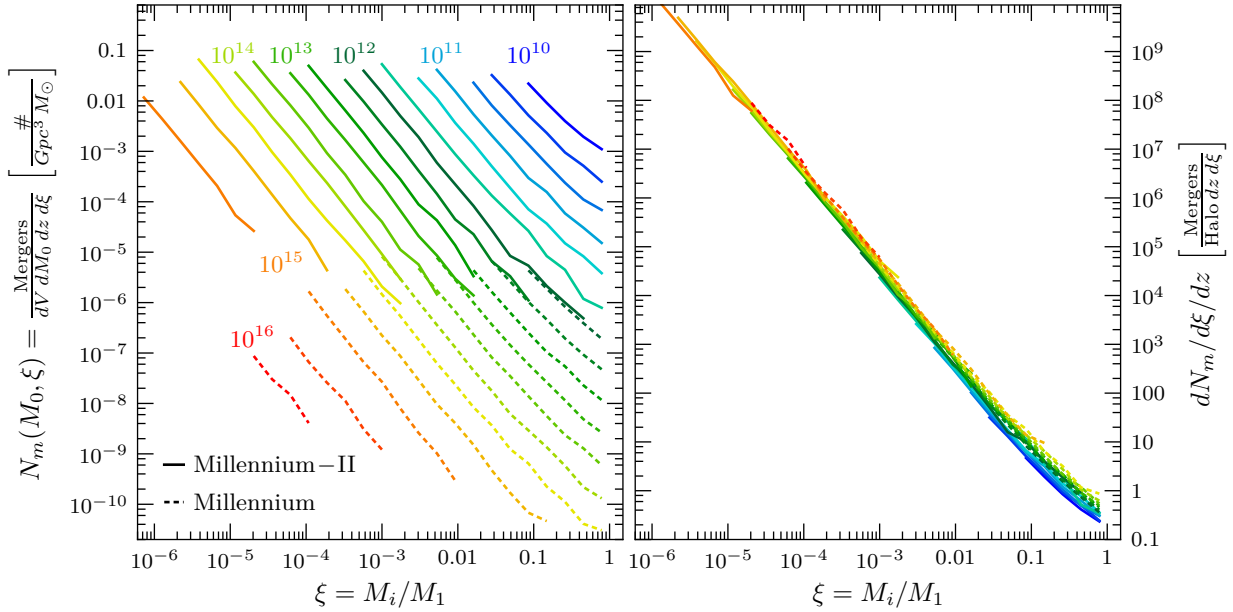


Figure 1. Left panel: The mean merger rate of $z = 0$ FOF haloes, $B(M_0, \xi)$, as a function of the mass ratio of the progenitors (ξ) and the descendant halo mass (M_0) over 6 orders of magnitude: 10^{10} to $10^{16} M_\odot$ from right (blue) to left (red). The Millennium-II results are shown in solid, while the results from the Millennium are in dashed curves. Right panel: The mean merger rate *per halo*, $B(M_0, \xi)/n(M_0) \equiv dN_m/d\xi/dz$. Normalizing $B(M_0, \xi)$ by the halo number density $n(M_0)$ collapses the curves in the left panel to nearly a single curve, indicating that $dN_m/d\xi/dz$ is nearly independent of M_0 and has a simple universal form.

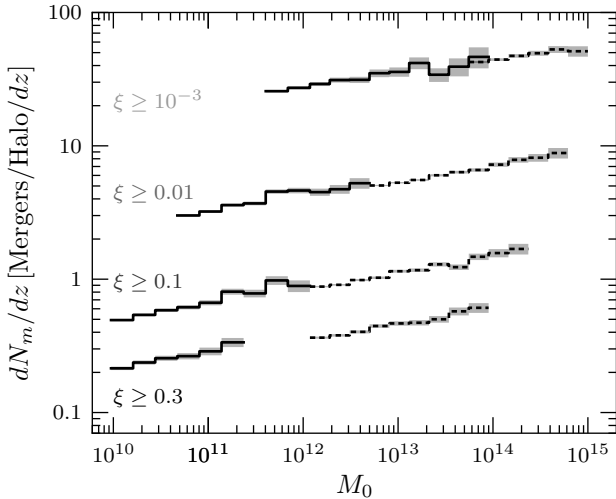


Figure 2. The $z \approx 0$ mean merger rate per halo (per unit z), dN_m/dz , as a function of descendant mass, M_0 , for four ranges of progenitor mass ratio ξ . The Millennium-II results are shown in solid, while the original Millennium results are the dashed curves. The upper curves include increasingly more minor mergers. The mass dependence is weak over five orders of magnitude in mass and is well approximated by a power law $\propto M_0^{0.133}$.

ing from major mergers with $\xi_{\min} = 0.3$ (solid curves at bottom), to extreme minor mergers with $\xi_{\min} = 10^{-5}$ (dotted curve at top). Within each line type, the colors indicate different descendant mass bins ranging from 10^{10} (blue) to $> 10^{14} M_\odot$ (red). Only the higher mass bins are plotted as ξ_{\min} is lowered. This is because minor mergers of low-mass haloes fall below the mass resolution limit.

Fig. 3 indicates that the general trends reported in

Fig. 8 of Fakhouri & Ma (2008) continue to hold in the Millennium-II Simulation. The dimensionless rate dN_m/dz is remarkably independent of redshift up to $z \sim 15$, whereas the rate per Gyr, dN_m/dt , rises with increasing z because a unit redshift corresponds to a shorter time interval at higher z . This redshift dependence is similar to that obtained by Guo & White (2008) for the dimensionless growth rates due to mergers of both haloes and galaxies (based on semi-analytic models) from the Millennium Simulation.

3.1.3 Merger Rate Fitting Forms

Since the merger statistics in Figs. 1-3 are very consistent between the two Millennium simulations, we use an analytical form similar to equation (12) of Fakhouri & Ma (2008) to fit the dimensionless mean merger rate $dN_m/d\xi/dz$ (in units of mergers per halo per unit redshift per unit ξ) from the combined Millennium dataset. An appealingly simple feature of this fitting form is that it is separable in the variables M_0 , ξ , and z :

$$\frac{dN_m}{d\xi dz}(M, \xi, z) = A \left(\frac{M}{10^{12} M_\odot} \right)^\alpha \xi^\beta \exp \left[\left(\frac{\xi}{z} \right)^\gamma \right] (1+z)^\eta. \quad (1)$$

We find the best-fit parameters to be $(\alpha, \beta, \gamma, \eta) = (0.133, -1.995, 0.263, 0.0993)$ and $(A, \xi) = (0.0104, 9.72 \times 10^{-3})$. The near z -independence in the left panel of Fig. 3 is more striking than in our 2008 study due to the larger coverage in redshift here. In view of this lack of z -dependence, we choose to use the simpler factor of $(1+z)^\eta$ here rather than the growth rate of the density field used in Fakhouri & Ma (2008). In comparison to our 2008 study, the power-law slope of the mass dependence is slightly steeper here ($\alpha = 0.133$ vs. 0.089), whereas the power-law slope of the ξ dependence

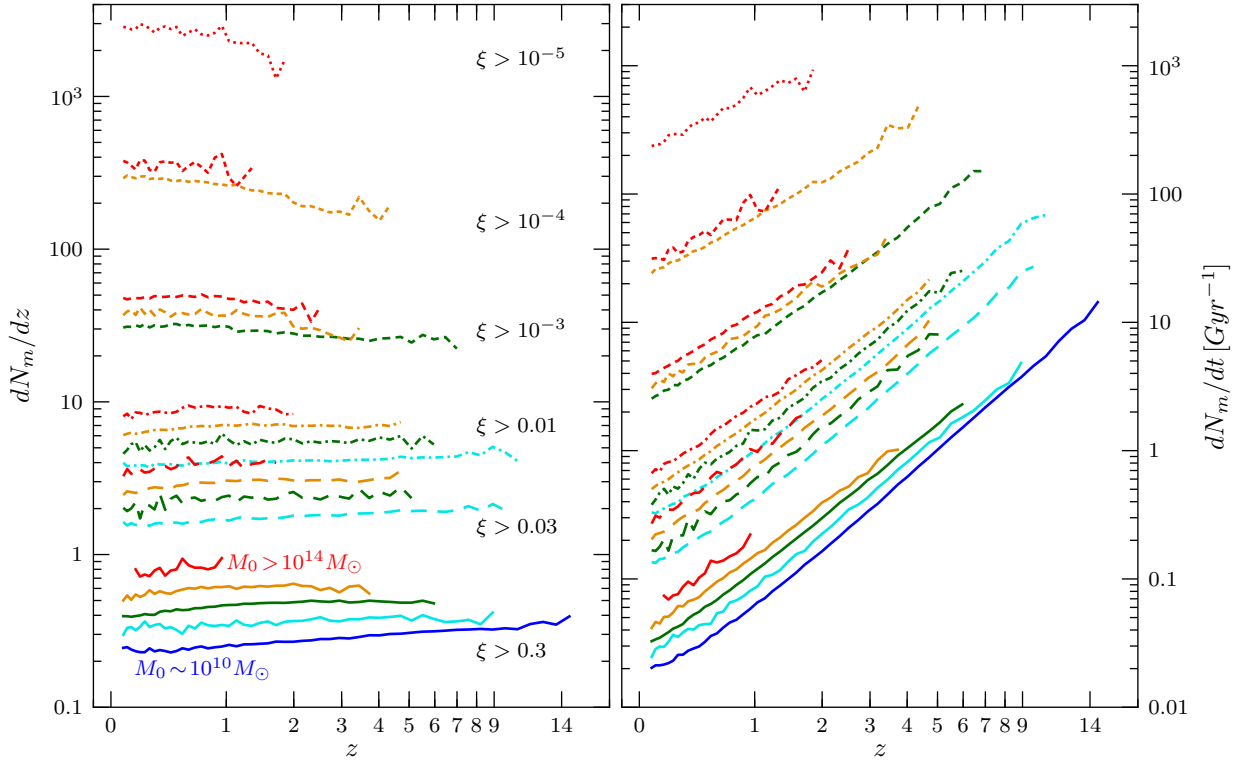


Figure 3. Time evolution of the mean halo merger rates *per halo* in units of per redshift, dN_m/dz (left panel), and in units of per Gyr, dN_m/dt (right panel) from the two Millennium simulations. The descendant mass M_0 and progenitor mass ratio ξ over five orders of magnitude are plotted. The weak dependence of the rates on M_0 is shown by the different colors: $\approx 10^{10}$ (blue), 10^{11} (cyan), 10^{12} (green), 10^{13} (orange), to $> 10^{14} M_\odot$ (red). The line types denote different types of mergers, ranging from major mergers (solid) to extreme minor mergers (dotted). The rate dN_m/dz on the left is remarkably constant out to $z \sim 15$; the rapid rise of dN_m/dt with increasing z on the right is therefore largely due to the cosmological factor dt/dz , which spans a shorter time per unit z with increasing z .

is slightly shallower here ($\beta = -1.995$ vs. -2.17). These differences are primarily due to the differing definitions of halo mass used in the two studies (FOF vs. sum of subhalos; see Sec. 2.4) and the refinements in our stitch-3 algorithm (see the Appendix).

We note that the left panel of Fig. 3 does show mild variations in the redshift dependence among the different ξ bins: the rate increases slightly with increasing z for major mergers, while it declines somewhat for the very minor mergers ($\xi_{\min} \sim 10^{-4}$ to 10^{-5}). Since this variation is so minor and the minor merger regime is more prone to numerical resolution issues, we have opted for simplicity rather than a more complicated fitting form.

3.2 Mass Growth Rates and Assembly Histories

In the last section, we presented results for the instantaneous rates of halo mergers as a function of redshift, descendant mass, and progenitor mass ratio. Here, we examine a related set of statistics that quantify the mass growth of haloes. These two quantities are clearly related since mergers are a primary process for haloes to gain mass, but mergers are not the only process. As discussed at length in Fakhouri & Ma (2010), “diffuse” accretion of unresolved haloes or dark matter particles also makes an important contribution to halo growth. In the mass assembly history of a halo, mergers with other haloes typically result in more discrete but less

frequent changes in the halo mass, while diffuse accretion leads to a more continuous change.

3.2.1 Mass Accretion Rates

To compute the total mass growth rate of a halo of a given mass M_0 at time t , we follow the main branch of its merger tree (see § 2.3) and set $\dot{M} = (M_0 - M_1)/\Delta t$, where M_0 is the descendant mass at time t and M_1 is the mass of its most massive progenitor at time $t - \Delta t$. The mean value of \dot{M} as a function of z for the complete set of resolved haloes in the two Millennium simulations is plotted in Fig. 4 (solid curves). Nine ranges of M_0 spanning five orders of magnitude ($10^{10} M_\odot$ to $10^{15} M_\odot$ from bottom up) are shown. Fig. 4 can be compared directly to Fig. 5 of McBride et al. (2009) for the Millennium Simulation alone. The rising $\langle \dot{M} \rangle$ with increasing redshift in our earlier study is seen to continue to $z \sim 14$, and the nearly linear scaling of $\langle \dot{M} \rangle$ with halo mass is extended down to $\sim 10^{10} M_\odot$.

We find the mass accretion rates shown in Fig. 4 to be very well fit by the forms given by equations (8) and (9) of McBride et al. (2009). The coefficients quoted there only need minor adjustments after the Millennium-II results are added. We suggest the following updated fits to the mean and median mass growth rates of haloes of mass M at red-

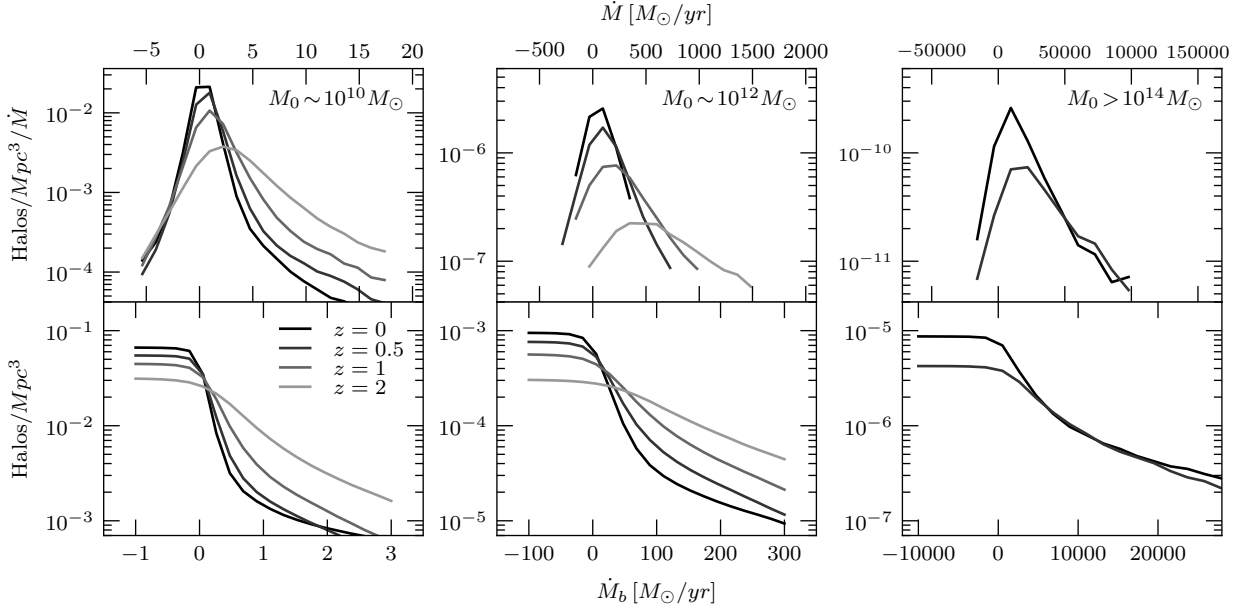


Figure 5. Differential (top) and cumulative (bottom) distributions of the baryonic accretion rates, \dot{M}_b , for halo masses 10^{10} (left), 10^{12} (middle), and $> 10^{14} M_\odot$ (right). Within each panel, the accretion rates at $z = 0, 0.5, 1$, and 2 are shown (except the right panel, where such massive haloes are present only at $z = 0$ and 0.5). The distributions are seen to broaden significantly with increasing z . The vertical axis in each of the bottom panels labels the number of haloes per comoving Mpc^3 that are accreting at a rate of \dot{M}_b or above.

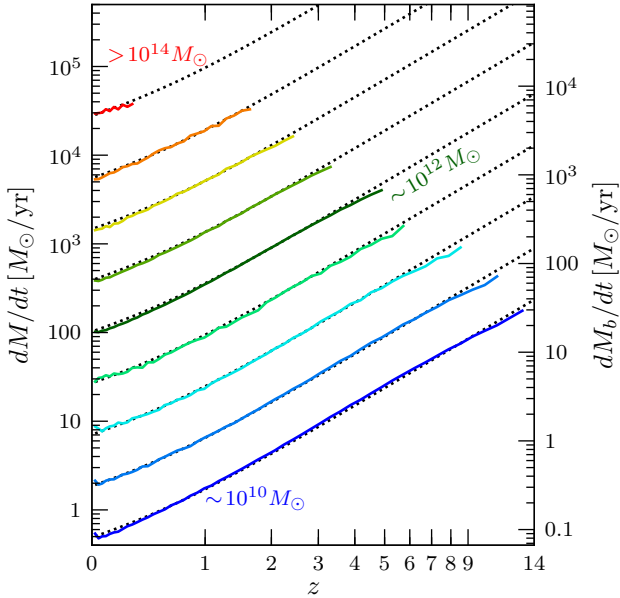


Figure 4. Mean mass accretion rate of dark matter onto haloes as a function of redshift from the two Millennium simulations (solid curves). Halo masses ranging from $10^{10} M_\odot$ to $> 10^{14} M_\odot$ are plotted. The dashed curves show the accurate fit provided by equation (2). The right-hand side of the vertical axis labels the mean accretion rate of baryons, \dot{M}_b , assuming a cosmological baryon-to-dark matter ratio of $1/6$.

shift z :

$$\begin{aligned}
 \langle \dot{M} \rangle_{\text{mean}} &= 46.1 M_\odot \text{yr}^{-1} \left(\frac{M}{10^{12} M_\odot} \right)^{1.1} \\
 &\quad \times (1 + 1.11z) \sqrt{\Omega_m (1+z)^3 + \Omega_\Lambda} \\
 \langle \dot{M} \rangle_{\text{median}} &= 25.3 M_\odot \text{yr}^{-1} \left(\frac{M}{10^{12} M_\odot} \right)^{1.1} \\
 &\quad \times (1 + 1.65z) \sqrt{\Omega_m (1+z)^3 + \Omega_\Lambda}.
 \end{aligned} \tag{2}$$

At a given mass and redshift, the mean rate is overall higher than the median rate since the distribution of \dot{M} has a long positive tail (see Fig. 5). The dashed curves in Fig. 4 illustrate the remarkable accuracy of this formula in matching the simulation results over the broad ranges of halo mass and redshift shown.

The right-hand-side label along the vertical axis of Fig. 4 shows the corresponding mean accretion rate of baryons, \dot{M}_b , where we have assumed a cosmological baryon-to-dark matter ratio of $\Omega_b/\Omega_m = 1/6$. These values are meant to provide a rough approximation for the mean rate at which baryons are being accreted near the virial radius of a dark matter halo. Most of these baryons are presumably in the form of warm or hot ionized hydrogen gas that is being channeled into the haloes along cosmic filaments, and various gas cooling and feedback processes will likely affect the baryon accretion rate. Many studies on galaxy formation are aimed at quantifying these physical processes under which these baryons are cooled to form neutral gas, molecular gas, and stars, and the feedback processes that heat up the baryons and lead to large-scale outflows.

In Fig. 5 we show the differential (top) and cumulative (bottom) *distributions* of the baryonic accretion rate for three halo masses (left to right panels) and four redshifts. A cosmic ratio of $\Omega_b/\Omega_m = 1/6$ is again assumed to convert the dark matter rate into a baryonic rate. The distributions are strongly peaked at the mean values presented in Fig. 4 but exhibit long tails towards high positive values due to major merger events and towards negative values due to tidal stripping and halo fragmentation. Not only is the mean accretion rate higher at higher z , the distribution of \dot{M}_b is also broader at higher z . For example, the comoving density of Milky Way-mass haloes that are accreting baryons at a rate of at least $100 M_\odot$ per year is approximately ten

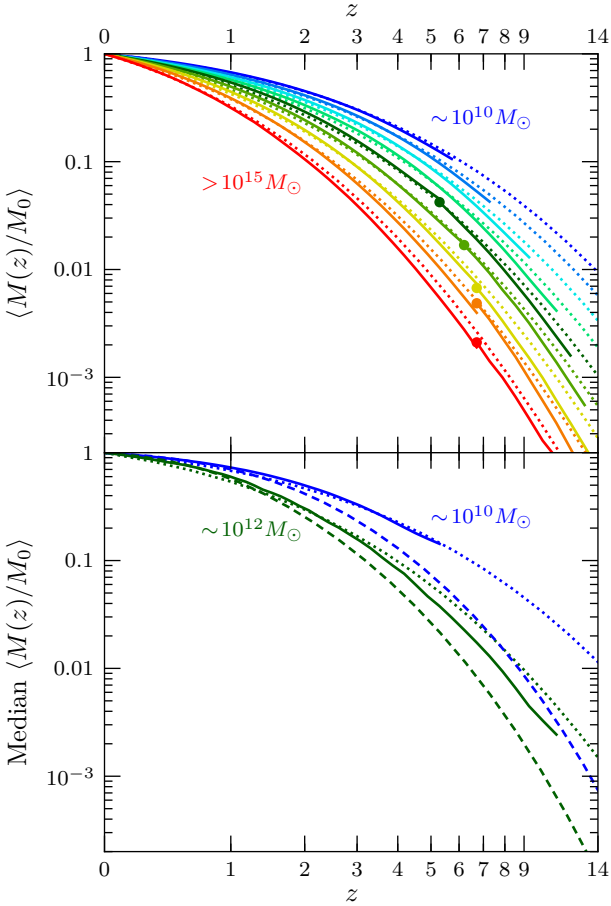


Figure 6. Top panel: Mean mass assembly history $M(z)$ of all $z = 0$ resolved dark matter haloes in the two Millennium simulations (solid curves). Nine ranges of halo mass from $10^{10} M_\odot$ (top blue) to $10^{15} M_\odot$ (bottom red) are plotted. The dotted curves show the predictions given by integrating the mean \dot{M} of our fitting formula (eq. 2). The lower four mass bins contain only haloes from the Millennium-II Simulation. For the upper five mass bins in which the haloes are drawn from both simulations, we use a solid circle to label the redshift above which only Millennium-II haloes contribute since the Millennium Simulation can no longer resolve haloes at such high z . The relatively smooth connection at the circle illustrates the consistency between the two simulations. Lower panel: Median mass assembly history $M(z)$. For clarity, only two mass bins are plotted. Solid lines are from the simulations, dotted lines from the integration of the mean \dot{M} from eq. (2), and dashed lines show the fits from Zhao et al. (2009).

times greater at $z = 2$ ($\sim 2 \times 10^{-4} \text{ Mpc}^{-3}$) than at $z = 0$ ($\sim 3 \times 10^{-5} \text{ Mpc}^{-3}$).

3.2.2 Mass Assembly Histories

The top panel of Fig. 6 shows the mean mass assembly history $M(z)$ for nine bins of M_0 (at $z = 0$) from 10^{10} to $> 10^{14}$ (from top to bottom). The solid curves show the results obtained from the main branch (i.e. the most massive progenitor) along the merger tree for all the $z = 0$ haloes in the two Millennium simulations. The dotted curves show the $M(z)$ obtained from integrating the fitting formula for the mean \dot{M} in equation (2) from the present-day to some

redshift z . The agreement is generally very good, in particular at $z \lesssim 8$. A perfect agreement is not expected because the two quantities, \dot{M} and $M(z)$, are not determined from the same set of haloes in the simulations: the \dot{M} statistics are obtained from all haloes of a given mass M at a given z , whereas the $M(z)$ curves show only the mean mass of the most massive progenitors at redshift z for the $z = 0$ haloes of mass M , which are a small subset of the haloes of the same mass that are present at z in the simulation boxes. In view of this difference, the agreement between the solid and dotted curves in the top panel of Fig. 6 is in fact quite remarkable. Over the large range of mass and redshift shown in Fig. 6, we have checked that the direct fits for the mean $M(z)$ proposed in recent literature (e.g. Boylan-Kolchin et al. 2009; McBride et al. 2009) provide a good match at low z , but integrating the fit for $\langle \dot{M} \rangle$ in equation (2) provides a closer match at high z ,

The solid curves in the bottom panel of Fig. 6 show the median, rather than the mean, mass assembly history obtained from the simulations for two mass bins centered at $M_0 = 10^{10} M_\odot$ and $10^{12} M_\odot$. We note that integrating our fit to the median \dot{M} does not yield the median $M(z)$ because unlike the mean \dot{M} , the median and derivative operations do not commute. The median and mean $M(z)$ are sufficiently similar, however, that we find integrating our mean \dot{M} to yield relatively good agreement with the median $M(z)$ (dotted curves). For comparison, the fit of Zhao et al. (2009) to the median $M(z)$ is shown as dashed curves. Their fit appears to be systematically lower than the Millennium results at $z > 1$.

In principle, we can integrate the (mass-weighted) halo merger rate in equation (1) and obtain the portion of the dark matter accretion rate $\langle \dot{M} \rangle$ in equation (2) that is due to mergers. As emphasized in Fakhouri & Ma (2010), however, accretion of “diffuse” material (consisting of unresolved haloes and tidally stripped mass) also makes a non-negligible contribution to $\langle \dot{M} \rangle$; equation (2) therefore can not be obtained solely from equation (1).

3.3 Merger Statistics over a Halo’s History

In the last two sections we quantified the halo merger rates, the mass growth rates, and the assembly histories of haloes. These quantities can be combined to predict a number of additional useful merger statistics over a halo’s history.

3.3.1 Cumulative number of mergers

One such statistic is $N_m(\xi_{\min}, M_0, z_0, z)$, the total number of mergers that a halo of mass M_0 at redshift z_0 has encountered between z_0 and an earlier z . The mergers can be characterized by major or minor mergers by imposing a limit of ξ_{\min} on the progenitor mass ratio (evaluated at the redshift of the merger). These numbers are essential for making theoretical predictions of galaxy properties that are impacted by mergers, e.g., the dynamics and stability of stellar disks, the star formation rate, and the color and morphology transformation due to mergers.

Fig. 7 shows $N_m(\xi_{\min}, M_0, z_0, z)$ for the complete set of resolved haloes at $z_0 = 0$ (left), 1 (middle), and 2 (right) from the two Millennium simulations. In each panel, five

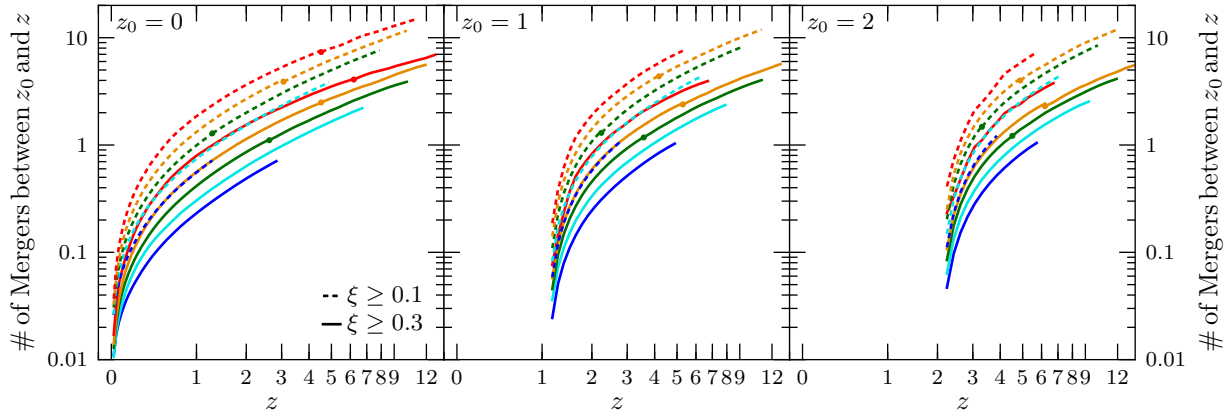


Figure 7. Mean number of mergers between redshifts z_0 and z experienced by a halo at $z_0 = 0$ (left), 1 (middle), and 2 (right) from the joint dataset of the two Millennium simulations. In each panel, the solid and dashed curves represent mergers with a progenitor mass ratio (defined at the time of merger) of $\xi \geq 0.3$ and $\xi \geq 0.1$. For each mass ratio cutoff, five ranges of halo mass are shown (from bottom up): 10^{10} (blue), 10^{11} (cyan), 10^{12} (green), 10^{13} (orange), and $> 10^{14} M_\odot$ (red). The lower-mass haloes are from the Millennium-II Simulation, whereas the cluster mass haloes are mainly from the Millennium Simulation. For mass bins in which the haloes are drawn from both simulations, we use a solid circle to label the redshift above which only Millennium-II haloes contribute since the Millennium can no longer resolve haloes at such high z . The fact that the curves connect quite smoothly are another indication of the consistency between the two simulations.

ranges of M_0 are plotted for redshift up to 12. Major mergers with $\xi \geq 0.3$ are shown by solid curves, while the more minor mergers with $\xi \geq 0.1$ are shown in dashed curves.

Fig. 7 shows that the mean trend of the number of mergers experienced over a halo’s lifetime is a sensitive function of the halo mass and merger mass ratio. haloes of Milky-Way mass at the present day (green curves) have on average experienced one major merger event ($\xi \geq 0.3$) per halo since $z \approx 2.3$, and one merger with $\xi \geq 0.1$ per halo since $z \approx 1$. When extended to $z \approx 7$, these haloes have on average encountered ~ 3 mergers with $\xi \geq 0.3$, and ~ 7 mergers with $\xi \geq 0.1$. The formation redshifts as well as the last merger epoch for more massive haloes are both lower, a well-known trend in CDM-based cosmology (see, e.g., Lacey & Cole 1993, 1994). Cluster-sized haloes with $M_0 \sim 10^{14} M_\odot$, for instance, have on average experienced one major merger event since $z \approx 1.2$, and one merger with $\xi \geq 0.1$ since $z \approx 0.6$.

It is possible to compute the cumulative number of mergers, $N_m(\xi_{\min}, M_0, z_0, z)$, shown in Fig. 7 from the fitting formula for the merger rate $dN_m/d\xi/dz$ in equation (1) and the mass accretion history $M(z)$ obtained by integrating $\langle \dot{M} \rangle$ in equation (2). Specifically, these quantities are related by

$$N_m(\xi_{\min}, M_0, z_0, z) = \int_{z_0}^z dz \int_{\xi_{\min}}^1 d\xi \frac{dN_m}{d\xi dz}(M(z), \xi, z). \quad (3)$$

Since we are interested in the number of mergers over a halo’s past history, we must take into account the fact that a halo’s mass generally decreases with increasing z , and that the merger rate depends on the halo mass (albeit weakly). The merger rate $dN_m/d\xi/dz$ at redshift z in the integrand above therefore should be evaluated using the mean mass $M(z)$ that a halo of mass M_0 at z_0 had at the earlier z . The results are shown in Fig. 8, which is identical to the left panel of Fig. 7 except that we have added the theoretical curves (thin curves) for comparison. The agreement with

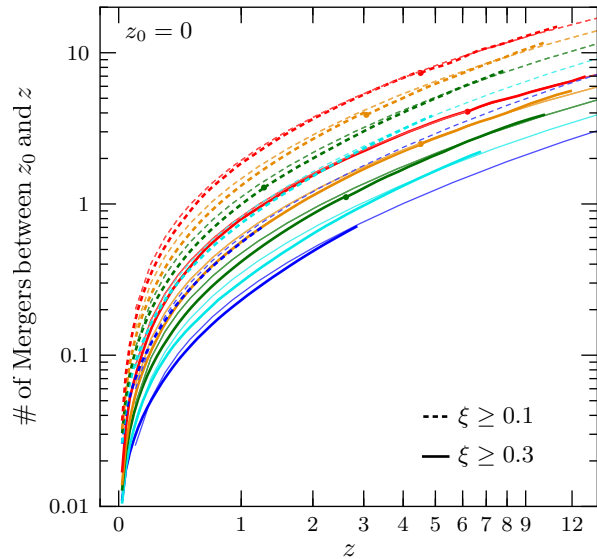


Figure 8. Same as the left panel of Fig. 7, with the addition of the predictions (thin curves) computed from eq. (3). The agreement with the simulation results (thick curves) is excellent, suggesting that eq. (3) can be used to make analytic predictions for merger statistics over a halo’s history.

the simulation results (thick curves) is excellent, suggesting that equation (3) can be used to make analytic predictions for merger statistics over a halo’s history.

3.3.2 Redshift of last major merger

The redshift at which each curve in Fig. 7 crosses one merger event along the vertical axis is a useful quantity since it gives the mean redshift at which a halo has experienced its last major merger (LMM). The LMM redshift of a halo is closely

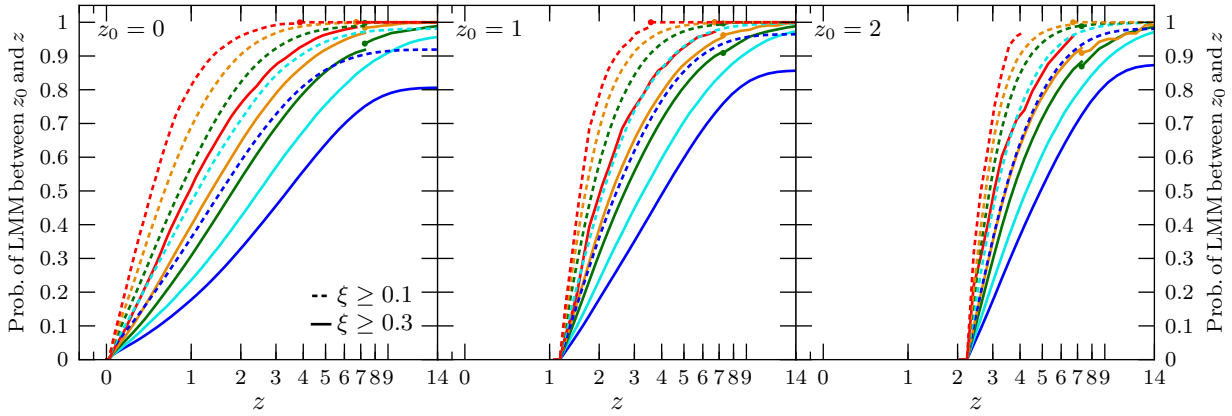


Figure 9. Cumulative distribution of the redshift at which the last (i.e. most recent) major merger occurred in a halo’s past history for haloes at $z_0 = 0, 1,$ and 2 (left to right) in the two Millennium simulations. The vertical axis gives the probability that the last major merger occurred between z_0 and redshift z . The curves are defined the same way as in Fig. 7.

related to its formation redshift and may be linked to the time at which the associated galaxy last experienced prominent star formation activity and morphological changes. To analyze this quantity further, we show in Fig. 9 the *distribution* of the LMM redshift for haloes at $z_0 = 0, 1,$ and 2 (from left to right). Within each panel, five halo masses and two ranges of ξ are plotted. The vertical axis gives the probability that a halo at a given z_0 has had a last major merger between z_0 and z .

Useful merger statistics can be read off from Fig. 9. For instance, 50% of present-day haloes have had a major merger ($\xi \geq 0.3$) since $z \approx 1, 1.8,$ and 3.4 for halo mass $10^{14}, 10^{12},$ and $10^{10} M_\odot$, respectively. When more minor mergers with $\xi \geq 0.1$ are considered, the median redshift of the last merger is lowered to $0.4, 0.8,$ and 1.6 for the three masses. The assembly history of Milky Way-size haloes is of particular interest; see Boylan-Kolchin et al. (2009) and references therein for a detailed statistical study of this topic. For haloes of $M_0 \sim 10^{12} M_\odot$ today, the left panel of Fig. 9 shows that $\sim 31\%, 53\%,$ and 69% of these haloes have experienced a major merger since $z = 1, 2,$ and 3 , respectively. For haloes of $\sim 10^{12} M_\odot$ at $z_0 = 1$ (middle panel), about 50% of them have had a major merger since $z \approx 2.7$, and for haloes of the same mass at $z_0 = 2$ (right panel), about 50% of them have had a major merger since $z \approx 3.7$.

4 SUMMARY AND CONCLUSIONS

We have combined the halo catalogs from the two Millennium simulations to form an unprecedentedly large dataset for studying the merger statistics and assembly histories of dark matter haloes in the Λ CDM cosmology. The two simulations provide, respectively, 11.3×10^6 haloes (between redshift 0 and 6) and 7.5×10^6 haloes (between redshift 0 and 15) above 1000 particles for our study. These haloes and their merger trees have allowed us to determine the dark matter halo merger rates and mass growth rates from $z = 0$ to up to $z = 15$, for over five orders of magnitude in the descendant halo mass ($10^{10} \lesssim M_0 \lesssim 10^{15} M_\odot$) and progenitor mass ratio ($10^{-5} \lesssim \xi \leq 1$). For the small range of overlap-

ping parameter space between the two simulations, we have found the agreement to be excellent.

For the merger rates, the basic features reported in our earlier study based on the Millennium Simulation alone (Fakhouri & Ma 2008) are largely preserved in the Millennium-II Simulation. The mean merger rate *per halo*, $dN_m/d\xi/dz$, is nearly independent of the descendant mass (Fig. 1 and 2) and scales as $\propto M_0^{0.133}$ at all redshifts. The merger rate in units of per redshift is nearly independent of redshift out to $z \sim 15$ (left panel of Fig. 3); the rate in units of per Gyr is therefore largely determined by the cosmological factor of dt/dz and increases roughly as $(1+z)^{2.5}$ at $z \gtrsim 1$ (right panel of Fig. 3). Equation (1) provides an update on our simple analytical fitting form for the merger rate as a function of $M_0, \xi,$ and z .

For the mass growth rates of individual haloes, we have found the mean and median statistics (Fig. 4) to be well approximated by the simple fitting form of our earlier study (McBride et al. 2009). The updated coefficients based on the joint dataset from the two Millennium simulations are given by equation (2). The present-day mean and median rates at which a $10^{12} M_\odot$ dark matter halo is accreting mass (at the virial radii) are 46.1 and $25.3 M_\odot \text{ yr}^{-1}$, respectively. This rate increases nearly linearly with the halo mass, and increases with redshift approximately as $(1+z)^{1.5}$ at low z and $(1+z)^{2.5}$ at $z \gtrsim 1$.

We have also presented statistical quantities that track the merger histories of dark matter haloes cumulatively. Fig. 7 presents the number of major mergers experienced by haloes of various mass between redshift z_0 and z for $z_0 = 0, 1,$ and 2 . Fig. 9 presents the probability that a dark matter halo at redshift z_0 will have last experienced a major merger at some earlier redshift z . Much interesting and useful information regarding the contribution to halo growth made by major mergers can be read off these figures with ease.

With the addition of results from the Millennium-II Simulation to our previous analysis of the Millennium Simulation, the merger rate of dark matter haloes is now well-quantified for haloes with masses between 10^{10} and $10^{15} M_\odot$ for redshifts $z \lesssim 15$, modulo the uncertainties inherent in halo definitions and in algorithms for handling fragmenta-

tion (see Appendix), for the cosmology used in the Millennium simulations. Several avenues remain open for future work, however.

One obvious extension of the results in this paper is to consider the mergers of *subhaloes* themselves, as subhalo mergers can be more directly linked to galaxy mergers than can FOF halo mergers (Angulo et al. 2009; Wetzel et al. 2009). Furthermore, the structure of the merger trees produced for the Millennium simulations lends itself naturally to computing subhalo merger properties. While computing subhalo merger rates and connecting them to galaxy mergers presents additional challenges – in particular, the issues of assigning stellar masses to subhaloes, numerical resolution effects, and subhalo identification within larger FOF haloes – a thorough theoretical understanding of such rates is essential for disentangling the relative contributions of merging and star formation to the growth of galaxies.

ACKNOWLEDGEMENTS

The Millennium Simulation databases used in this paper and the web application providing online access to them were constructed as part of the activities of the German Astrophysical Virtual Observatory.

APPENDIX: COMPARISON OF DIFFERENT FOF MERGER TREES

We refer the reader to Section 5 and Figure 8 of Fakhouri & Ma (2009) for a detailed discussion of the three basic operations – “snip,” “stitch,” and “split” – that we have implemented and tested for handling the issue of halo fragmentations during the construction of a merger tree for FOF haloes (see also Section 2.2 of this paper). Briefly, “snip” removes halo fragmentation events by severing the ancestral link between the fragment subhalo and its progenitor, “stitch” places the fragment subhalo back into the FOF halo from which it emerged, whereas “split” removes the fragment subhalo’s progenitor from its FOF halo, thereby generating a new FOF at the progenitor redshift.

Within the stitch and split algorithms, the operations can be applied either on a subset of fragments or on all fragments in a given FOF tree. We therefore subdivide each algorithm into two: stitch- ∞ vs stitch-3, and split- ∞ vs split-3. The stitch- ∞ and split- ∞ algorithms perform the given operation on all FOF fragments. This is done recursively from the redshift of fragmentation, going forward in redshift for stitch- ∞ , and backwards in redshift for split- ∞ , until there are no more fragments present in the simulation merger trees. As a result of this recursive process, stitch- ∞ identifies the first (highest- z) snapshot in which two subhaloes join the same FOF to be their merger time, whereas split- ∞ selects the last (lowest- z) snapshot.

These algorithms introduce some complications, however. One particular problem faced by split- ∞ is the fact that there exists a firm cutoff at $z = 0$, beyond which we do not have merger or fragmentation information. As a result, although a fragment may actually finally merge beyond $z = 0$, split- ∞ will incorrectly assign its final merger to an earlier redshift. This results in a pile-up of merger events

at $z = 0$ and, as we will show, artificially raises the low- z merger rate with respect to the high- z rate. Since there is no analogous hard limit at high z , stitch- ∞ does not suffer from this same behavior, and fragment mergers are re-distributed across all high redshifts evenly. On the other hand, any chance encounter between subhaloes that results in the FOF algorithm spuriously linking them together is interpreted as a real merger event by stitch- ∞ . The subhaloes, which may never interact again, are nonetheless forced to join the same FOF group down to $z = 0$.

The stitch-3 and split-3 algorithms are designed to limit the propagation effects of stitch- ∞ and split- ∞ . Stitch-3 performs the stitching operation on any FOF fragment that is observed to remerge with its progenitor FOF’s main branch within 3 snapshots of the fragmentation event. Any fragments that do not satisfy this criterion are snipped, resulting in an orphan halo that may or may not later remerge. The split-3 algorithm performs the split operation on any FOF fragment that is *not* a member of the main branch FOF at some point in the 3 snapshots *before* the fragmentation event. Again, fragments that do not satisfy this criterion are snipped.

Neither stitch-3 nor split-3 adequately removes all re-merger events. Depending on the context this may be either a weakness or a strength: although the notion of halo re-mergers may be considered as multiple counting from a theoretical perspective, observers will likely count as signatures all events that trigger mergers, regardless of whether they are the first or last entry.

Moreover, both split-3 and stitch-3 have superior time convergence properties to the snip algorithm, in which the re-merger problem is entirely unmitigated. Thus, stitch-3 and split-3 stand as intermediates between the snip and stitch- ∞ /split- ∞ algorithms.

An immediate concern is whether the halo mass function is heavily modified by the destruction/creation of FOFs due to the stitch/split operations. We have verified that these operations do not modify the mass function severely. For stitch-3 and split-3, the deviations are within 3% of the unprocessed mass function at all redshifts, while deviations of up to 10% exist for the stitch- ∞ (split- ∞) algorithm at low (high) redshifts.

Fig. 10 compares the five post-processing algorithms directly by presenting ratios of the per-halo merger rate, $dN_m/d\xi/dz$, as a function of progenitor mass ratio ξ at five redshifts ($z = 0.06, 0.5, 1, 2,$ and 4 from top bottom). Each column presents the ratio of the merger rate of a particular post-processing algorithm (left to right: snip, stitch-3, stitch- ∞ , split- ∞) to the merger rate extracted from the split-3 trees presented throughout this paper. Different mass bins are presented by different colored curves ranging from $10^{10} M_\odot$ (blue) to $10^{15} M_\odot$ (red). We note that though the region of overlap between Millennium (dashed) and Millennium II (solid) is small, there appears to be smooth continuation between these two sets of curves for all post-processing algorithms.

The merger rates computed by all algorithms converge towards high z , though there is some residual disagreement with split- ∞ and snip at the $\sim 20\%$ level. There are, however, distinct systematic differences among the algorithms when $z < 4$. Since we presented stitch-3 as our algorithm of choice for handling halo fragmentation in Fakhouri & Ma

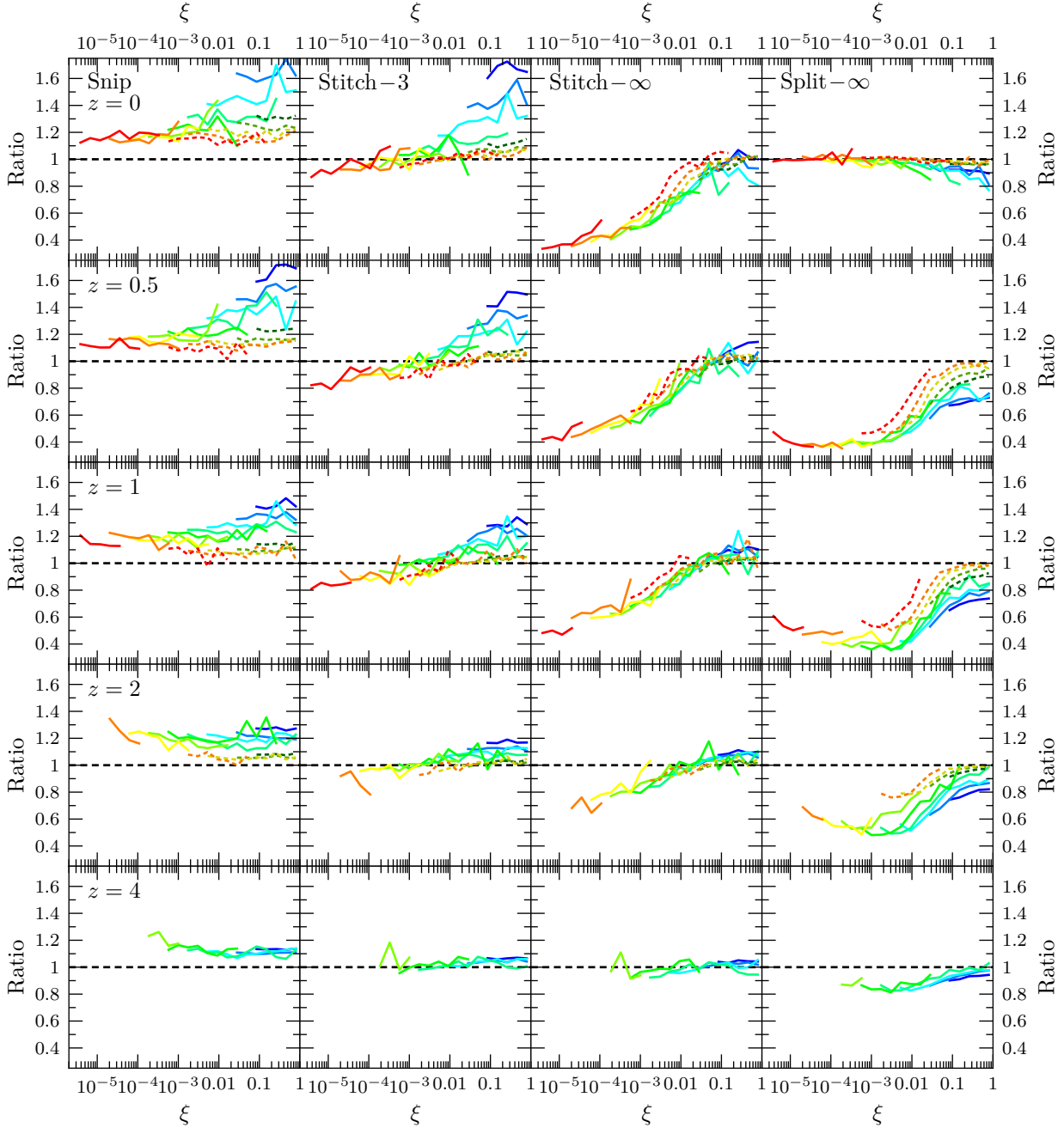


Figure 10. Comparison of five algorithms used to handle halo fragmentation events in the FOF merger trees: snip, stitch-3, stitch- ∞ , split- ∞ , and split-3. Results presented throughout this paper are based on the split-3 tree. Plotted as a function of the progenitor mass ratio ξ (left to right) are the ratios of the merger rates, $dN_m/d\xi/dz$, between each of the first four algorithms relative to the split-3 results. Five redshifts are shown: $z = 0, 0.5, 1, 2$ and 4 (top to bottom). Within each panel, up to nine mass bins are shown: $10^{10}M_\odot$ (blue) to $> 10^{14}M_\odot$ (red). The Millennium Simulation results are presented with dashed curves and Millennium II with solid curves. The systematic differences amongst the five algorithms are discussed in the text.

(2008), we focus on the comparison of stitch-3 and split-3 in this section. The origins of the differences between the other algorithms and split-3 can be inferred from the discussion of the algorithms earlier in this section.

The second column of Fig. 10 shows that stitch-3 and split-3 are in excellent agreement at all ξ for high mass haloes ($M_0 > 10^{12}$). Low mass haloes, however, can show significant deviations in the merger rate. This is true especially in

the major merger regime, where the merger rate predicted by stitch-3 is over 50% higher than split-3. This distinction was not detectable using Millennium alone, as the mass resolution limited our analysis to $M_0 \geq 10^{12}M_\odot$.

To understand this deviation we have studied a subset of halo mergers in detail by analyzing halo tracks, velocities, and merger histories. In particular, we have constructed a number of criteria to determine whether a given merger is

actually a spurious encounter: if the relative velocity of the two haloes greatly exceeds the more massive halo's maximum circular velocity, if the angle between the velocity vectors of the two haloes exceeds 70° at the time of merger, or if the FOF algorithm only associates the two haloes for two snapshots out of the eight snapshots centered on the merger snapshot, then the merger is deemed spurious. A qualitative look at three-dimensional halo trajectories finds that this criteria does a good job of identifying chance halo encounters and premature mergers.

For halo mergers with $1.1 \times 10^{10} < M_0 < 1.3 \times 10^{10}$ and $\xi > 0.1$ at $z = 0$, we find that stitch-3 identifies 1,304 mergers, while split-3 only identifies 738 mergers. Of these, 505 mergers are in common, leaving split-3 with 233 mergers that are not in stitch-3 and stitch-3 with 799 mergers that are not in split-3. Of the 505 mergers in common, only 4 (0.8%) are deemed spurious by our criterion. Similarly, of the 233 mergers unique to split-3, only 12 (5.2%) are deemed spurious. Of the 799 mergers unique to stitch-3, however, 589 (73.7%) are deemed spurious. These spurious mergers are primarily comprised of chance encounters in which the two otherwise unassociated haloes merge for a snapshot or two and then disconnect. While split-3 correctly splits these events, stitch-3 does not and consequently inflates the merger rate. When these spurious mergers are removed, the remaining 210 mergers unique to the stitch-3 algorithm bring the stitch-3 and split-3 rates into close agreement.

We note that depending on the context, one may choose one algorithm over another. Stitch- ∞ provides the *first* encounter merger rate, but is known to link chance-encounter haloes that should not be linked. Split- ∞ provides the *last* encounter merger rate, but cannot be trusted for $z < 1$ and may incorrectly underpredict the merger rate due to spurious fragmentation. Split-3 stands in between both algorithms: it does not propagate up and down the tree and does not heavily modify the distribution of FOFs, but it does double count some halo remerger events. This may be odious to the theorist, but may yield the most appropriate merger rate for comparison to observation.

REFERENCES

Angulo R. E., Lacey C. G., Baugh C. M., Frenk C. S., 2009, MNRAS, 399, 983
 Berrier J. C., Bullock J. S., Barton E. J., Guenther H. D., Zentner A. R., Wechsler R. H., 2006, ApJ, 652, 56
 Boylan-Kolchin M., Springel V., White S. D. M., Jenkins A., 2009, arXiv:0911.4484 [astro-ph]
 Boylan-Kolchin M., Springel V., White S. D. M., Jenkins A., Lemson G., 2009, MNRAS, 398, 1150
 Cole S., Helly J., Frenk C. S., Parkinson H., 2008, MNRAS, 383, 546
 Davis M., Efstathiou G., Frenk C. S., White S. D. M., 1985, ApJ, 292, 371
 Fakhouri O., Ma C., 2010, MNRAS, 401, 2245
 Fakhouri O., Ma C.-P., 2008, MNRAS, 386, 577
 Fakhouri O., Ma C.-P., 2009, MNRAS, 394, 1825
 Genel S., Genzel R., Bouché N., Naab T., Sternberg A., 2009, ApJ, 701, 2002

Gottlöber S., Klypin A., Kravtsov A. V., 2001, ApJ, 546, 223
 Governato F., Gardner J. P., Stadel J., Quinn T., Lake G., 1999, AJ, 117, 1651
 Guo Q., White S. D. M., 2008, MNRAS, 384, 2
 Lacey C., Cole S., 1993, MNRAS, 262, 627
 Lacey C., Cole S., 1994, MNRAS, 271, 676
 Li Y., Mo H. J., van den Bosch F. C., Lin W. P., 2007, MNRAS, 379, 689
 Maller A. H., Katz N., Kereš D., Davé R., Weinberg D. H., 2006, ApJ, 647, 763
 McBride J., Fakhouri O., Ma C., 2009, MNRAS, 398, 1858
 Springel V., 2005, MNRAS, 364, 1105
 Springel V., White S. D. M., Jenkins A., Frenk C. S., Yoshida N., Gao L., Navarro J., Thacker R., Croton D., Helly J., Peacock J. A., Cole S., Thomas P., Couchman H., Evrard A., Colberg J., Pearce F., 2005, Nat, 435, 629
 Springel V., White S. D. M., Tormen G., Kauffmann G., 2001, MNRAS, 328, 726
 Springel V., Yoshida N., White S. D. M., 2001, New Astronomy, 6, 79
 Stewart K. R., Bullock J. S., Barton E. J., Wechsler R. H., 2009, ApJ, 702, 1005
 Stewart K. R., Bullock J. S., Wechsler R. H., Maller A. H., Zentner A. R., 2008, ApJ, 683, 597
 Tormen G., 1998, MNRAS, 297, 648
 Tormen G., Bouchet F. R., White S. D. M., 1997, MNRAS, 286, 865
 van den Bosch F. C., 2002, MNRAS, 331, 98
 Wechsler R. H., Bullock J. S., Primack J. R., Kravtsov A. V., Dekel A., 2002, ApJ, 568, 52
 Wetzel A. R., Cohn J. D., White M., 2009, MNRAS, 395, 1376
 Zhao D. H., Jing Y. P., Mo H. J., Börner G., 2009, ApJ, 707, 354